Ibn Al-Haitham Journal for Pure and Applied Sciences
Journal homepage: jih.uobaghdad.edu.iq
PISSN: 1609-4042, EISSN: 2521-3407
IHJPAS. 2025, 38(3)

Impacts of Non-Thermal Plasma on the Structural and Optical Characteristics of Cr:Se Core-Shell Thin Films Synthesized Using Chemical Spray Pyrolysis

Taghreed A. Hilmi[1] and Ramiz A. Al-Ansari[2*]
[1,2]Department of Physics, College of Science for Women, University of Baghdad, Baghdad, Iraq.
*Corresponding Author.

Received: 6 June 2024 Accepted:10 September 2024 Published: 20 July 2025
doi.org/10.30526/38.3.4026

Abstract

Over the past few years, there has been a significant focus on studying the synthesis and applications of metal nanoparticles. These tiny particles possess distinct properties that set them apart from bulk metals. Cr:Se core-shell nano thin film has been pre-coated by plasma jets with different concentrations (10:0, 8:2, and 6:4) and deposition by chemical spray pyrolysis. The nano-thin films were analyzed by X-ray diffraction (XRD), ultraviolet-visible spectroscopy(UV), and transmission electron microscopy TEM. This study looks into the structure and optical features of core-shell nanoparticles made with different ratios of chromium and selenium (Cr:Se). The X-ray diffraction patterns confirm the crystalline nature of the nanoparticles and the ratio (6:4). Exposing the best crystalline phase to non-thermal plasma (DBD) results in significant changes in the XRD, transitioning towards a more crystalline phase. Tauc plots show a non-linear trend in direct bandgap energies, meaning the energy gap increased (2.77-3.88 eV), notably increasing. Transmission electron microscopy analysis highlights improved nanoparticle distribution and uniformity. non-thermal plasma (DBD) significantly enhances the humidity sensitivity, thereby optimizing the nanoparticles for sensor applications. These findings underscore the potential of Cr:Se nanoparticles for advanced optoelectronic and sensing technologies and various technological applications.

Keywords: Cr:Se, Core-shell, Plasma jets, DBD, Thin film.

1. Introduction

The field of nanotechnology is rapidly expanding, allowing for the development of new materials and technologies with sizes in the nanometer range (1-100 nm) for a wide variety of uses(1). Scientists have been highly interested in nanomaterials because of their distinct properties in comparison to larger materials. Nanoparticles possess compact dimensions, expansive surface areas, and distinctive chemical and physical characteristics that render them well-suited for a multitude of applications (2). Plasma jet technology methods have become significant methods for nanoparticle synthesis (3) The technique of plasma jets has many advantages, including low cost, environmental friendliness, and no need for expensive equipment (4).

When it comes to protective coating applications, the outstanding hardness, wear resistance, and corrosion resistance of thin films are highly sought-after attributes. Chemical spray pyrolysis(5), reactive pulsed laser ablation, electrochemical deposition (6), electron beam evaporation, sputtering(7), Chemical vapor deposition (CVD) process (8). Some of the techniques for applying coatings. On the other hand, chrome (Cr) nanoparticles have found extensive applications and can influence dielectrics and magnetics (9). Chromium composites have extensive use in the production of various structural components, such as components for jet engines, tools, thermal screens, and beyond (10).

The industrial use of chromium metal pollutes the environment. Selenium (Se) NPs are more effective in solar cells. (11-13).Selenium can reduce toxicity (13). Core-shell nanoparticles also referred to as core-shell, shell, or core-shell(1, 14). These nanoparticles are a combination of different materials. The Core and Shell nanoparticles are created by forming a shell using two or more nanoparticles. One nanoparticle coats the surface of the core, while another nanoparticle acts as the core(15) . Physical and chemical methods have been used to generate nanoparticles for a variety of materials. (16) Numerous techniques, including chemical precipitation(17), sole gel, thermal breakdown, and pulsed laser deposition(18), can be used to create nanoparticles (19). Plasma is an ionization gas made up of various particles, such as positive and negative ions, electrons, atoms, molecules, radicals, and UV rays.

It is commonly referred to as the fourth state of matter (20). Various types of plasma, like plasma jet or remote plasma, can be used to create nanoparticles. A gas discharge occurs between an electrode and the electrolyte surface (21). Non-thermal plasma (NTP) generated through gas discharge has emerged as a highly researched field. Dielectric barrier discharges (DBDs) are widely used in various industries due to their ability to generate non-thermal plasmas (NTPs) at atmospheric pressure and different frequencies. These NTPs have proven to be valuable for surface modification, environmental protection, medical applications, and plasma displays. The advantage of DBDs is that they can achieve these results without the need for costly vacuum equipment.(22, 23) The primary objective of this research is to explore how the ratio of Cr to Se and the application of DBD treatment affect the structural and functional properties of Cr:Se nanoparticles. By understanding these relationships, we aim to optimize the nanoparticles for specific applications in optoelectronics and sensing technologies.

2. Materials and Methods

In this work, it has been prepared Cr:Se core-shell NPS with different ratios (10:0), (6:4), and (8:2) have been prepared by plasma jet (24) and deposition as thin films by chemical spray pyrolysis(25). Using the technique of plasma jet, nanoparticles were synthesized efficiently and quickly, offering numerous advantages. synthesized Cr:Se core-shell NPs by using a high-voltage, two electrodes made of stainless steel (a tube and a sheet), argon gas, and a flow meter set to 3 liters per minute. A DC power source with a high voltage between 20 and 25 KV. In addition, the electrodes and the gas are connected to the power supply anode “terminal” and positioned 1 cm above the liquid via a stainless steel hollow metal tube about 3 cm long **(Figure 1)**. From chromium “nitrate” solid $Cr(NO_3)_3$ and selenium nitrate $SeNO_3$, the concentration of the Cr:Se nanoparticles was determined by the equation below (26).

$$\text{Concentration (mole)} = \frac{\text{mass}}{\text{molecular weight}\left(\frac{\text{g}}{\text{mol}}\right)*\text{volume(liter)a}} \quad (1)$$

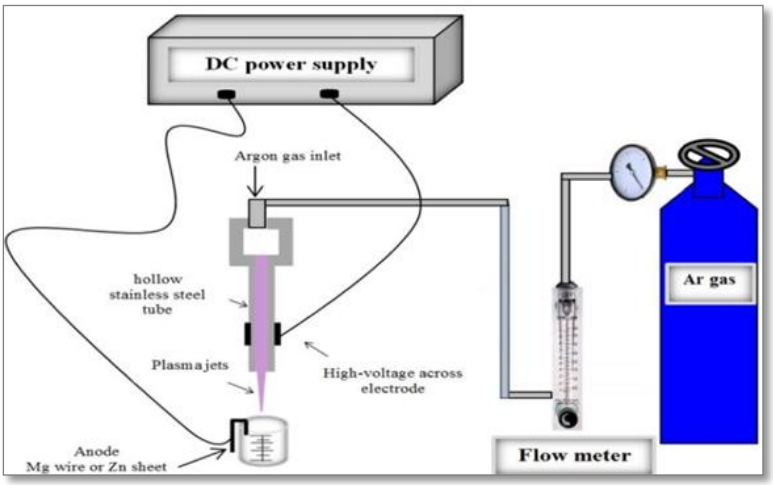

Figure 1. The Experimental Setup Of Cr:Se NP Synthesis By Plasma Jet

2.1. Core-Shell Synthesis

Nanoparticles with a core and a shell were synthesized in a two-step process. The first stage included creating Cr NPs, which were prepared by a plasma jet for 17 minutes. The color change assures that the liquid is a nanoparticle. Making the (Se) shell NPs that encase the (Cr) core NPs was the second stage. A variety of methods were used to characterize the produced Cr:Se nanoparticles **(Figure 2**).

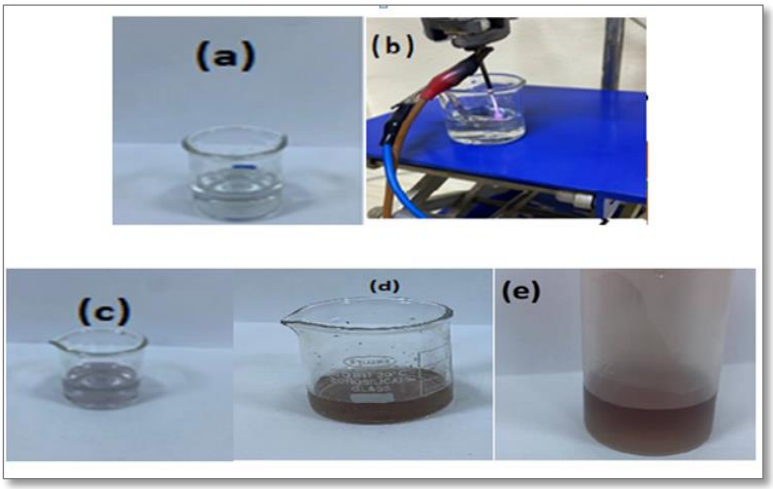

Figure 2. (a) $Cr(NO_3)_3$ with water **(b)** synthesis NPs by plasma jet **(c)** Cr NPs (10:0) **(d)** Cr :Se NPs (6:4) **(e)** Cr :Se NPs (8:2).

2.2. Deposition Thin Films

By the chemical spray pyrolysis method, Cr:Se Nps liquid was deposited on the glass. The steps of preparing the glass bases were first cleaning and second drying. The dimensions of the glass were 2.5*2.5 cm. Then the ratio (6:4) that was prepared by the plasma jet under 275 °C was used to spray it onto bases and glass. The ideal parameters were as follows: a base temperature of 275 °C, a vertical distance of about 29 cm between the sprayer and the device, an air pressure of 3 bars, and films that were created with good consistency. The pyrolysis rate is 2 ml/min, the spray duration is 5 seconds, and the stop time is 55 seconds, as indicated in **Figure (3)**.

XRD, scanning electron microscopy (SEM) analyses, and UV-vis spectrophotometers were conducted at the University of Technology, while transmission electron microscopy (TEM) analyses before and after DBD plasma were conducted at the University of Kashan in Iran.

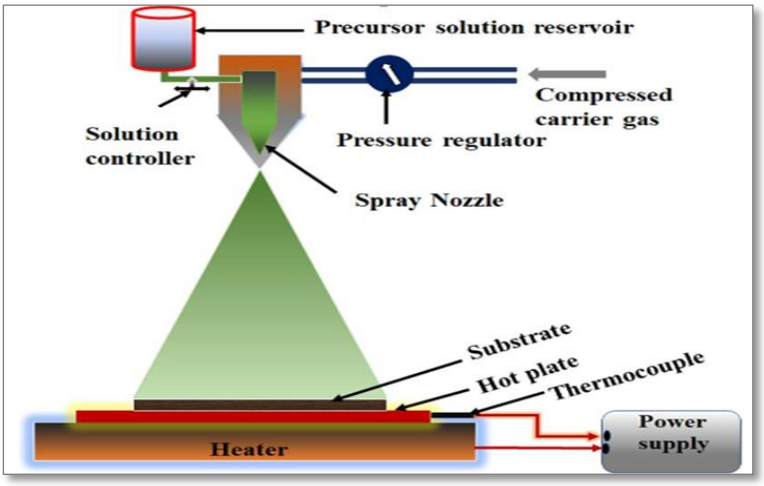

Figure 3. General schematic of a spray pyrolysis deposition process

2.3. Non-Thermal (DBD) Plasma Exposure

After preparation and study (structure and optical) properties of core-shell NPs by plasma jet and deposition on the substrate by chemical pyrolysis for a (6:4) ratio, and exposure by DBD plasma **Figure (4)** for 5 sec, it appears that there is a new structure and optical properties as shown below.

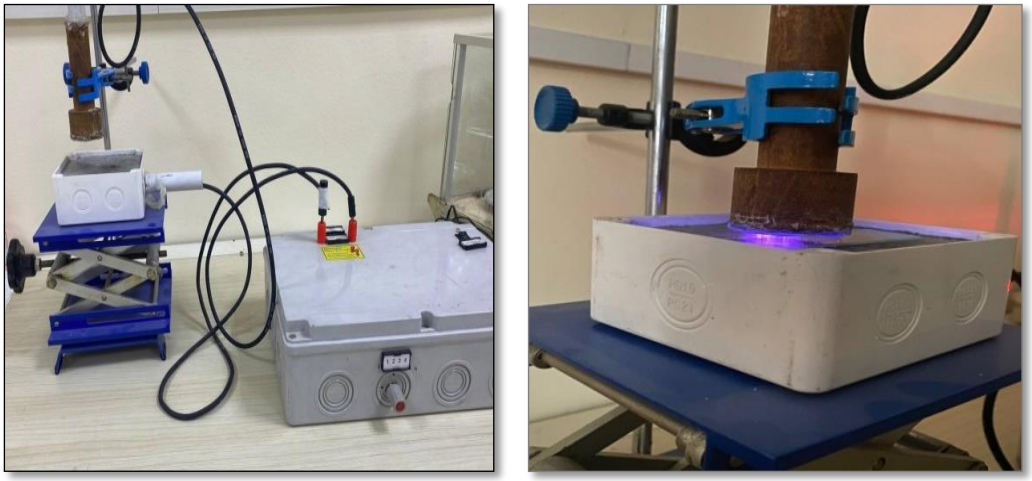

Figure 4. DBD plasma device and exposure thin film (6:4).

3. Results and Discussion

3.1. Structural properties

3.1.1. (X-Ray) Diffraction

The XRD pattern was recorded for(6:4) Cr:Se NPs after deposition of thin films by the spray pyrolysis method as a perfect ratio according to crystalline, the 2θ angle ranging from 10 to 80 for core and shell before and after DBD plasma, as **Figure (5)**. The curve represents the XRD pattern before DBD treatment, showing broad peaks indicative of a crystalline structure. The curve shows the XRD pattern after DBD treatment, which exhibits sharper peaks, suggesting a transition towards a more crystalline structure at 2θ = 24.48, 33.76, and 36.5; they can be assigned to (012), (014), and (110) according to JCPDS card no. 96-210-

4123(27). The peaks of Se at 2θ = 29.7°, 41.4°, and 43.7° were confirmed to be the Se-crystal planes of (101) (110), and (102), respectively, and the card no (JCPDS 9008579) was paired with these peaks(28). In **Figure (5),** after exposure, the intensity of the peaks increased (5 sec) in DBD plasma. Also, the crystalline size was evaluated by the following Debye-Scherrer's formula (29, 30).

$$D = \frac{K\lambda}{\beta \cos\theta} \quad (2)$$

where D: is the crystallite size, k: is the Scherrer's constant (k = 0.9), λ: is the X-ray wavelength, and β:- for full width at half maximum (FWHM) of the angles at which the peaks occur with Bragg's angle. It can be noted that (6:4) transfer about (51nm to 36 nm), these results are in good agreement with (31).

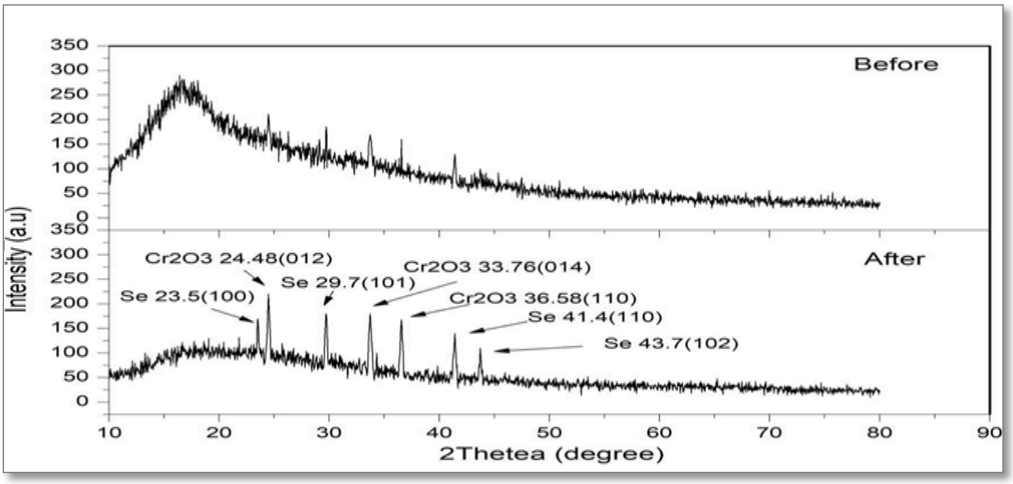

Figure 5. XRD pattern for Cr:Se NPs before and after DBD plasma.

3.2 TEM Analyses

The TEM images provide a comparative analysis of the optimized Cr:Se nanoparticles before and after DBD treatment. In the first set of images, depicting the nanoparticles before DBD treatment, the nanoparticles appear to be aggregated with irregular shapes and varying sizes. **Figure (6 a and b)** show clusters of particles with some degree of dispersion, but overall, the nanoparticles seem to form larger, denser clusters, indicating less uniformity and potential agglomeration.

In contrast, the second set of images, taken after DBD treatment, shows a notable change in the morphology and dispersion of the nanoparticles. Post-DBD treatment, the nanoparticles are more evenly distributed and exhibit a more uniform size and shape. **Figure (7 c and d)** reveal that the DBD treatment has resulted in a more homogeneous dispersion with fewer large aggregates. The nanoparticles appear to be better separated and more distinct, suggesting that the DBD treatment has effectively modified the surface properties of the nanoparticles, reducing agglomeration and promoting a more stable dispersion.

This comparative analysis indicates that DBD treatment significantly improves the morphological characteristics of Cr:Se nanoparticles, leading to enhanced dispersion and uniformity. These improvements are likely responsible for the observed increase in electrical conductivity and stability in the treated nanoparticles, as better-dispersed nanoparticles provide more effective charge transport pathways.

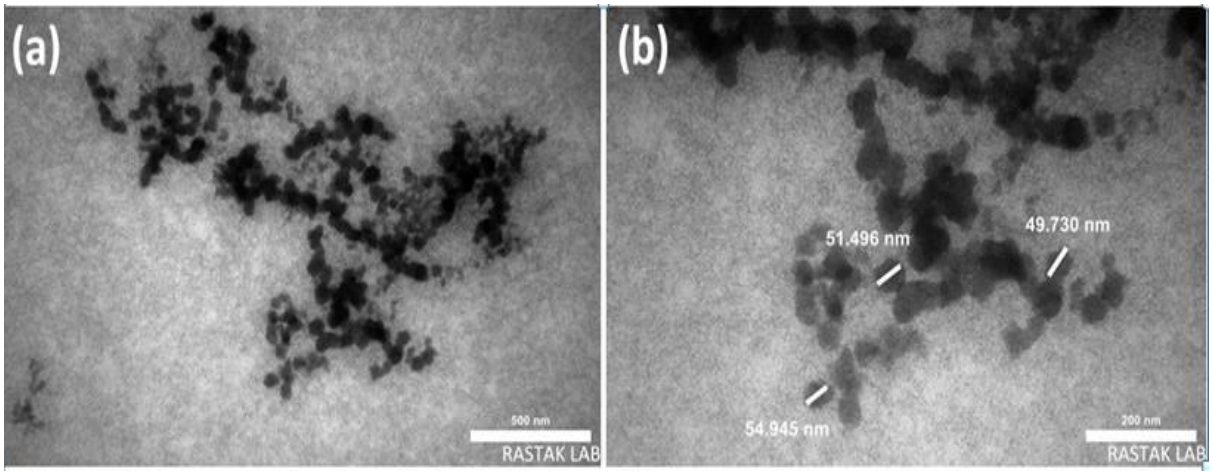

Figure 6. TEM images of the optimized Cr:Se nanoparticles before the DBD treatment.

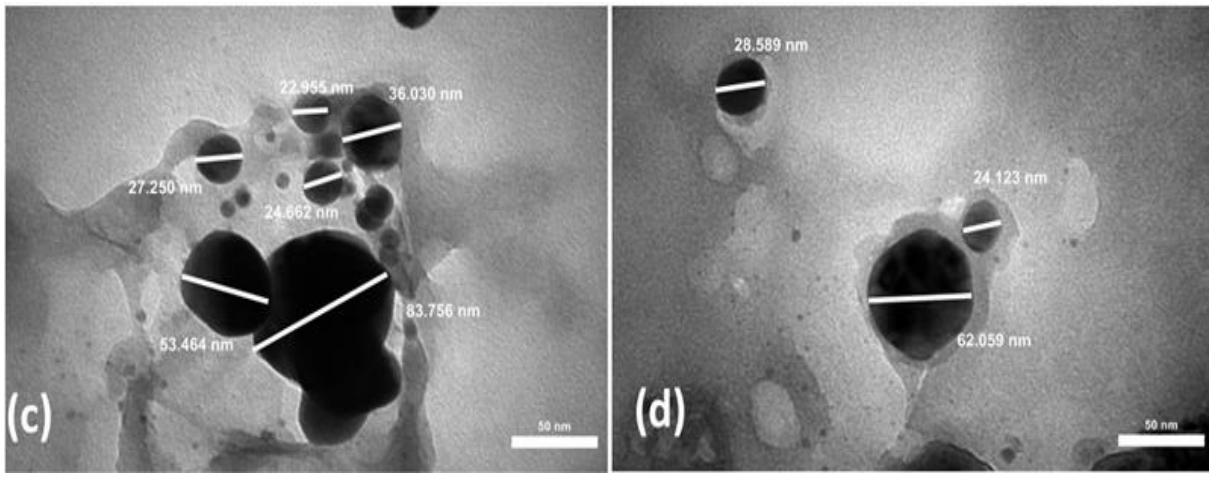

Figure 7. TEM images of the optimized Cr:Se nanoparticles after the DBD treatment

3.3. Optical Properties

3.3.1. Transmittance

Transmittance For core-shell nanoparticles with a size range of 290-800. The relationship between wavelength and the spectrum becomes more pronounced as the wavelength increases, as illustrated in **Figure (8)** and through it can be noted the difference between before and after DBD plasma. The rise in transmittance starts at a wavelength that is shorter than 400 nm. When the exposure to non-thermal plasma at time (5) sec, transmittance readings start to rise Gradually as the wavelength increases.

The increase begins at short wavelengths less than (400 nm) also ,That demonstrates the direct transitions. It has been observed that the highest transmittance occurs in the middle visible spectrums. Also to determine transmittance as the ratio of incoming light intensity (I_0) to the intensity of rays passing through the film (I_T).

$$T= I_T/I_0 \quad (3)$$

3.3.2. Absorption Constant (Σ)

Absorption is measured as a function of wavelengths based on the transmittance spectrum within the range (290- 800 nm) for (6:4) core-shell NPs before and after (DBD plasma) as shown in **Figure (9)**. The results show that the absorption is found to be reduced by increased wavelength due to a lack of photon energy and an inability to excite electrons irritate and move from the valence band to the conduction band. That is, the relationship is inverse between wavelength and photon energy. The absorption values begin to decrease after

exposure to non-thermal plasma at (5 sec) with increasing wavelength, to determine the absorption coefficient from equation (4).

$$\boldsymbol{\alpha} = 2.303\,\frac{A}{t} \quad (4)$$

Where: A = absorbance, t = Thickness

Also, understanding the thickness of the film factor is crucial, as it plays a significant role in determining the physical properties of the film. Using an optical interferometer method, the thickness of the Cr:Se (6:4) thin film was measured to be 158.9 nm. This was done by appointment with the HeNe laser with a wavelength of (0.632) μm and an incident angle of 45°. This method relies on the interference of the laser beam reflected from the surface of a thin film and the substrate. The thickness of the film (t) can be determined using the following formula:

$$d = \frac{\Delta x}{x} * \frac{\lambda}{2} \quad (5)$$

The formula contains:- x:- is fringe width, Δx:- is the distance between two fringes, λ:- is the wave wavelength of laser light.

3.3.3. Band Gab

The provided **Figure (10)** illustrates the Tauc plots for determining the direct energy bandgap of chromium-selenium (Cr:Se) nanoparticles (NPs) with a 6:4 ratio, both before and after DBD treatment.

$$\alpha h\upsilon = B_0\ (h\upsilon - Eg\ opt)^{r} \quad (6)$$

where α:- the absorption; h :- Planck's constant; υ :- incident photon frequency; B_0 :- constant about 0.9; E.g.:- the optical energy gap; and r :- exponential constant.

In **Figure (10)**, the plt displays $(\alpha h\nu)^2$ on the y-axis against energy (eV) on the x-axis, with the intercept of the linear portion of the plot indicating a direct energy bandgap of (2.77) eV before DBD treatment. Also shows the Tauc plot for the Cr:Se NPs after DBD treatment, where the linear extrapolation intersects the energy axis at a higher value, revealing an increased direct bandgap energy of 3.88 eV. This significant increase in direct bandgap energy, from 2.77 to 3.88 eV, suggests that DBD treatment effectively alters the electronic properties of the Cr:Se NPs. The enhancement in bandgap energy could be attributed to changes in the material structure, such as a reduction in defect states, alteration in particle size, or surface passivation effects that diminish the density of states in the band tail region. Consequently, the increase in bandgap energy implies that the material will now absorb light at shorter wavelengths (higher energies), enhancing its suitability for applications in optoelectronics and photovoltaics. Furthermore, a larger bandgap generally indicates a lower intrinsic carrier concentration at room temperature, impacting the conductivity and carrier mobility of the material. In summary, the DBD treatment has resulted in a substantial increase in the direct bandgap energy of Cr:Se nanoparticles, significantly altering their electronic and optical properties and potentially improving their performance in specific technological applications.

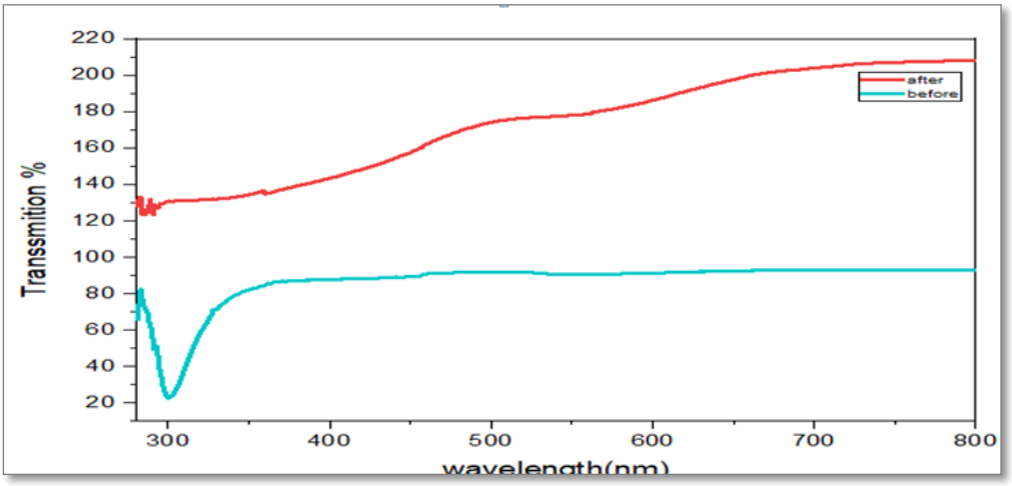

Figure 8. Optical Transmission for Cr:Se (6:4)NPs

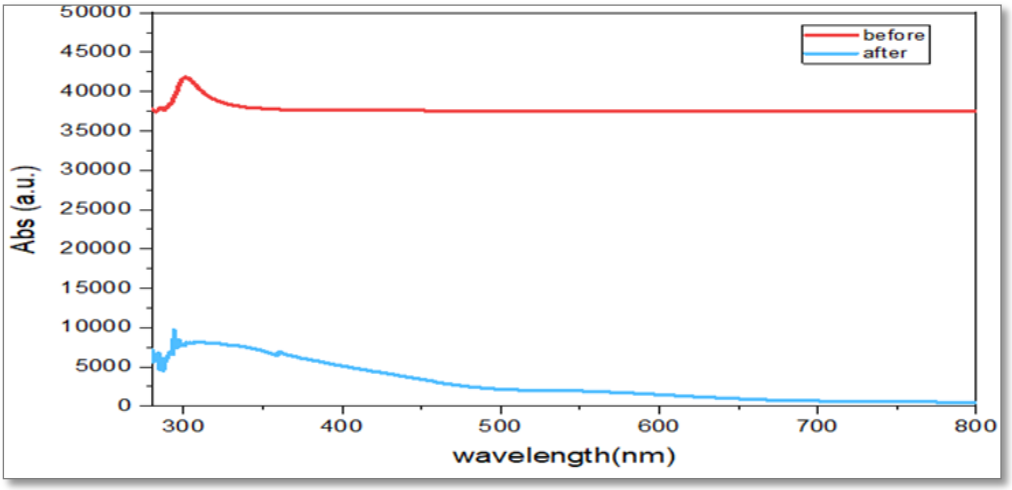

Figure 9. Absorption coefficient

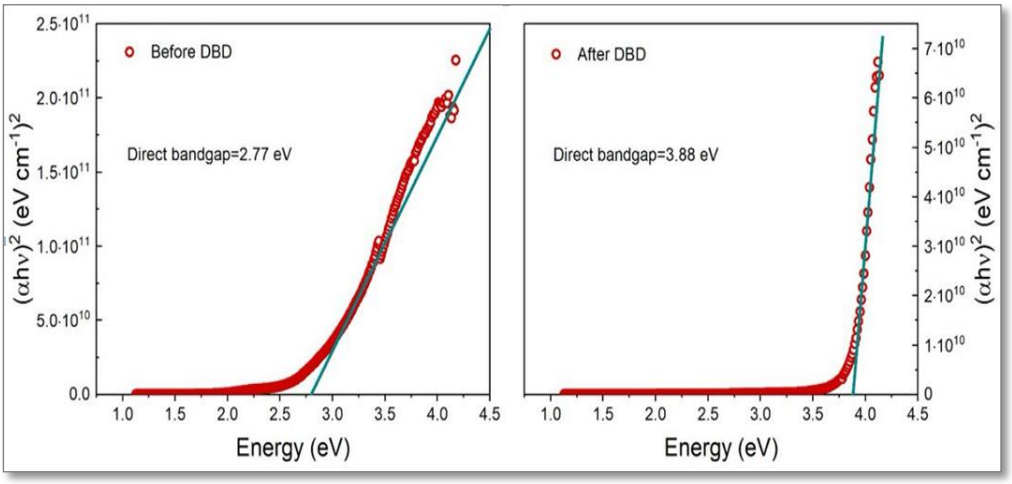

Figure 10. Energy band gaps of Cr:Se nanoparticles with a 6:4 ratio. Conjugation causes an increase in the bandgap energy.

4. Conclusion

The comprehensive analysis of Cr:Se nanoparticles thin film with varying Cr ratios highlights their potential for advanced material applications, particularly in optoelectronics and sensor technologies. XRD patterns confirm the crystalline nature of the nanoparticles, with significant structural reorganization observed post-DBD treatment, indicating a

transition towards more crystallinity. UV-Vis spectra and Tauc plots reveal changes in electronic properties, with a notable increase in bandgap energy after DBD treatment, enhancing the nanoparticles' suitability for high-energy applications TEM analysis demonstrates improved nanoparticle dispersion and uniformity post-DBD treatment, contributing to enhanced electrical conductivity and humidity sensitivity. Overall, this study provides a strong framework for tuning the structural and functional properties of Cr nanoparticles, making the way for their integration into various technological applications.

Acknowledgment

Thanks to the University of Baghdad, College of Science for Women, Department of Physics**.**

Conflict of Interest

Not Found.

Funding

None.

References

1. Ghosh Chaudhuri R, Paria S. Core/shell nanoparticles: classes, properties, synthesis mechanisms, characterization, and applications. Chem Rev. 2012;112(4):2373–2433. https://doi.org/10.1021/cr100449n
2. Habibullah GJ, Viktorova T. Current strategies for noble metal nanoparticle synthesis. Nanoscale Res Lett. 2021;16(1):47. https://doi.org/10.1186/s11671-021-03480-8
3. Nguyen LN. Structural and optical sensing properties of nonthermal atmospheric plasma-synthesized polyethylene glycol-functionalized gold nanoparticles. Nanomaterials. 2021;11(7):1678. https://doi.org/10.3390/nano11071678
4. Bisht S. Plasma applications for environmental protection. Int J Eng Adv Technol. 2014;3(5):77–81. https://doi.org/28d6a8f084e88872c1207bc97
5. Saleh KM. Study influence of substrate temperature on optical properties of CdS thin films prepared by chemical spray pyrolysis. Ibn Al-Haitham J Pure Appl Sci. 2019;32(1):7–16. https://doi.org/10.30526/32.1.1982
6. Bedolla-Hernández M. Electrodeposition mechanism of chromium nanoparticle coatings: modeling and experimental validation. Chem Eng Sci. 2022;252:117291. https://doi.org/10.1016/j.ces.2021.117291
7. Folkenant M. Structure and properties of Cr–C/Ag films deposited by magnetron sputtering. Surf Coat Technol. 2015;281:184–192. https://doi.org/10.1016/j.surfcoat.2015.09.054
8. Zhu X. Spin glass state in chemical vapor-deposited crystalline Cr2Se3 nanosheets. Chem Mater. 2021;33(10):3851–3858. https://doi.org/10.1021/acs.chemmater.1c01222
9. Azeez NA. Nano-remediation of toxic heavy metal contamination: Hexavalent chromium [Cr (VI)]. Chemosphere. 2021;266:129204. https://doi.org/10.1016/j.2020.129204
10. Mahmoud ME. Recent advances in adsorptive removal and catalytic reduction of hexavalent chromium by metal–organic frameworks composites. J Mol Liq. 2022;347:118274. https://doi.org/10.1016/j.molliq.2021.118274
11. Kolay A. Selenium nanoparticle-decorated silicon nanowires with enhanced liquid-junction photoelectrochemical solar cell performance. J Phys Chem C. 2019;123(14):8614–8622. https://doi.org/10.1021/acs.jpcc.9b00062
12. Kanagaraj J. Biosorption of trivalent chromium from wastewater: an approach towards green chemistry. Chem Eng Technol. 2014;37(10):1741–1750. https://doi.org/10.1002/ceat.201200716

13. Zhang B. Selenium (IV) alleviates chromium (VI)-induced toxicity in the green alga Chlamydomonas reinhardtii. Environ Pollut. 2021;272:116407. https://doi.org/10.1016/j.envpol.2020.116407
14. Khatami M, Alijani HQ, Sharifi I. Biosynthesis of bimetallic and core-shell nanoparticles: their biomedical applications–a review. IET Nanobiotechnol. 2018;12(7):879–887. https://doi.org/10.1049/iet-nbt.2017.0308
15. Gawande MB. Core-shell nanoparticles: synthesis and applications in catalysis and electrocatalysis. Chem Soc Rev. 2015;44(21):7540–7590. https://doi.org/10.1039/C5CS00343A
16. Parauha YR, Sahu VD. Prospective of combustion method for preparation of nanomaterials: A challenge. Mater Sci Eng B. 2021;267:115054. https://doi.org/10.1016/j.mseb.2021.115054
17. Rajput N. Methods of preparation of nanoparticles—a review. Int J Adv Eng Technol. 2015;7(6):1806. file:///C:/Users/hp/Downloads/Nano3%20(3).pdf
18. Hrdlicka M. Optical parameters of In–Se and In–Se–Te thin amorphous films prepared by pulsed laser deposition. J Phys Chem Solids. 2007;68(5–6):846–849. https://doi.org/10.1016/j.jpcs.2007.02.043
19. Afzal A. Structural and magnetic phase transition of sol–gel-synthesized Cr2O3 and MnCr2O4 nanoparticles. J Sol-Gel Sci Technol. 2016;80:96–102. https://doi.org/10.1007/s10971-016-4066-4
20. Rappaport WD. Effect of electrocautery on wound healing in midline laparotomy incisions. Am J Surg. 1990;160(6):618–20. https://doi.org/10.1016/s002-9610(05)80757-3
21. Maguire P. Continuous in-flight synthesis for on-demand delivery of ligand-free colloidal gold nanoparticles. Nano Lett. 2017;17(3):1336–1343. https://doi.org/10.1021/acs.nanolett.6b03440
22. Palaskar S. Dielectric barrier discharge plasma induced surface modification of polyester/cotton blended fabrics to impart water repellency using HMDSO. J Appl Polym Sci. 2011;122(2):1092–100. https://doi.org/10.1002/app.34237
23. De Geyter N. Effect of electrode geometry on the uniformity of plasma-polymerized methyl methacrylate coatings. Prog Org Coat. 2011;70(4):293–299. https://doi.org/10.1016/j.porgcoat.2010.11.009
24. Al-Halbosiy M. Effect gold nanoparticles generated by cold plasma for mineral blood. AIP Conf Proc. 2020; https://doi.org/10.1063/5.0032718
25. Patil PS. Versatility of chemical spray pyrolysis technique. Mater Chem Phys. 1999;59(3):185–98. https://doi.org/10.1016/S0254-0584(99)00049-8
26. Mohammed MS. Plasma jet prepared gold and silver nanoparticles to induce caspase-independent apoptosis in digestive system cancers. Mater Sci Forum. 2022; https://doi.org/10.4028/www.scientific.net/MSF.1050.51
27. Khalaji D. Structural, Optical and Magnetic Studies of Cr2O3 Nanoparticles Prepared by Microwave-Assisted. Nanochem Res. 2021;6(1):18–24. https://doi.org/10.22036/NCR.2021.01.003
28. Jiang FW, Cai G. Facile synthesis and optical properties of small selenium nanocrystals and nanorods. Nanoscale Res Lett. 2017;12:1–6. https://doi.org/10.1186/s11671-017-2165-y
29. Abdul-Ameer ZN. Novel Co-Precipitation method for synthesis of nanostructured nickel oxide in accordance to pH: Structural and optical properties as an active optical filter. Ibn Al-Haitham J Pure Appl Sci. 2019;32(1):1–6. https://doi.org/10.30526/32.1.1974
30. El-Nahas S. Controlled morphological and physical properties of ZnO nanostructures synthesized by domestic microwave route. Mater Chem Phys. 2021;258:123885. https://doi.org/10.1016/j.matchemphys.2020.123885
31. Dawood M. Effect of Li doping on structure and optical properties of NiO nano thin-films by SPT. AIP Conf Proc. 2020; https://doi.org/10.1063/5.0000136